![White Rose university consortium logo — Universities of Leeds, Sheffield & York]

eprints@whiterose.ac.uk
https://eprints.whiterose.ac.uk/

Optically pumped GeSn Microdisk Lasers on Si

Daniela Stange,[1]*[†] Stephan Wirths,[1]*‡ Richard Geiger,[2]*‡ Christian Schulte-Braucks,[1] Bahareh Marzban,[3]

Nils von den Driesch,[1] Gregor Mussler,[1] Thomas Zabel,[2] Toma Stoica,[1,4] Jean-Michel Hartmann,[5] Siegfried

Mantl,[1] Zoran Ikonic,[6] Detlev Grützmacher,[1] Hans Sigg,[2] Jeremy Witzens,[3] and Dan Buca[1][†]

[1]Institute of Semiconductor Nanoelectronics, Peter Grünberg Institute (PGI 9) and JARA-Fundamentals of

Future Information Technologies, Forschungszentrum Jülich, 52428, Germany

[2]Laboratory for Micro- and Nanotechnology (LMN), Paul Scherrer Institute, CH-5232 Villigen,

Switzerland

[3]Institute of Integrated Photonics, RWTH Aachen, 52074 Aachen, Germany

[4]National Institute of Materials Physics, P.O. Box MG-7, Magurele, Bucharest 077125, Romania

[5]Univ. Grenoble Alpes, F-38000 Grenoble, France and CEA, LETI, MINATEC Campus, F-

38054 Grenoble, France

[6]Institute of Microwaves and Photonics, School of Electronic and Electrical Engineering,

University of Leeds, Leeds LS2 9JT, United Kingdom

*These authors contributed equally

†Corresponding authors

Abstract: The strong correlation between advancing the performance of Si microelectronics and their demand of low power consumption requires new ways of data communication. Photonic circuits on Si are already highly developed except for an eligible on-chip laser source integrated monolithically. The recent demonstration of an optically pumped waveguide laser made from the Si-congruent GeSn alloy, monolithical laser integration has taken a big step forward on the way to an all-inclusive nano-photonic platform in CMOS. We present group IV microdisk lasers with significant improvements in lasing temperature and lasing threshold compared to the previously reported non-undercut Fabry-Perot type lasers. Lasing is observed up to 130 K and with optical excitation density threshold of 220 kW/cm^2 at 50 K. Additionally the influence of strain relaxation on the band structure of undercut resonators is discussed and allows the prove of laser emission for a just direct Ge$_{0.915}$Sn$_{0.085}$ alloy where Γ and L valley have the same energies. Moreover, the observed cavity modes are identified and modeled.

Keywords: GeSn, Group IV, Silicon Photonics, Microdisk, IR-Laser, strain engineering

Despite rapid progress made in the field of Silicon Photonics (SiP), the monolithic integration of an efficient group IV laser source has remained an outstanding and elusive goal for several decades[1]. Heterogeneous integration based on bonding of III-V materials[2–4] as well as epitaxial growth on Si wafers[5] has been intensively explored as a path forward to generate light on a Silicon (Si) chip. However, a photonic integrated circuits (PIC) solution based on group IV hetero-epitaxial growth of a suitable complementary metal-oxide-semiconductor (CMOS) compatible material carries the potential for drastic cost reduction and higher yield, as has already

2

been exemplified with Germanium (Ge) based photodetectors.[6] In recent years, the wavelength range supported by group IV integrated photonics devices has been extended to longer wavelengths with waveguides, detectors and modulators working in between 2-3 µm[7,8]. With Si-based lasers at hand, high volume applications like chip-to-chip optical interconnects within supercomputers, switches or high-performance servers[9] as well as consumable chips with sensors for point-of-care diagnostics[10,11] would greatly benefit from a fully functional CMOS compatible PIC technology.[12] Moreover, it will allow for the integration of lasers on the same Si chip and thus for the embedding of photonic architectures into Si microtechnology.[13,14]

Besides its technological and socio-economic impact, and in spite of promising steps made in the last few years,[15] the realization of a group IV integrated light source poses fascinating scientific challenges in order to overcome the physical limitation of the fundamental indirect bandgap group IV elements Si and Ge to efficiently generate light. Great efforts have been made to modify these materials, e.g. by applying tensile strain and/or by forming alloys,[16–19] in order to obtain a direct band gap. Here, Ge plays an essential role, since the energy difference between the conduction band Γ-valley at the center of the Brillouin zone and the L-valleys, the energetically lowest conduction bands, is only 140 meV. Currently the most successful route has been to alloy Ge with semi-metallic α-Tin (Sn). It has been concluded that the indirect-to-direct bandgap transition can be obtained in strain-free GeSn alloys (cubic lattice) by incorporating approx. 9 at.% Sn substitutionally into Ge,[19] or at constant Sn content by tuning the compressive strain in the crystal.[20] This achievement enabled the demonstration of optical gain and lasing in optically

3

pumped, partially strain relaxed $Ge_{0.875}Sn_{0.125}$ Fabry-Perot cavities at a wavelength of 2.3 µm and temperatures up to 90 K.[19]

While the Fabry-Perot waveguide cavities[19] enabled access to study the modal gain, the microdisk cavity arrangements are advantageous to engineer the strain. For instance, Ge microdisks with in-plane biaxial tensile strain have been realized using Si_3N_4 stressor layers. Photoluminescence (PL) and electroluminescence have been characterized on these Ge microdisks, however, without evidence of stimulated emission.[21,22] Recently, GeSn microdisk resonators were presented[23] showing whispering-gallery-mode (WGM) resonances. The investigated layer stack consisted of $Ge/Ge_{0.92}Sn_{0.08}/Ge$ quantum wells pseudomorphically grown on a sacrificial Ge layer. Although the energy difference between the Γ- and L-valleys could be reduced by introducing 8 at.% Sn and, hence, the quantum efficiency increased, the material remained a fundamental indirect semiconductor and, consequently, showed no gain.

In this article, microdisk cavities fabricated from our established GeSn gain material[19,20] are studied regarding their potential for group IV lasers. Following the description of the design and processing we discuss the spatial distribution of the residual strain over the microdisks and give the resulting energy levels of the electronic bands. The optical characterization yields the laser threshold intensities, its temperature dependence and the mode pattern. From a comparison between samples with a different Sn concentration and microdisks prepared with different amount of strain relaxations, the effect of the energy difference between L- and Γ-valleys on the lasing threshold is discussed.

RESULTS AND DISCUSSION

Laser design and processing using selective dry etching. The GeSn epilayers are grown on Ge-buffered (thickness 2.5 µm) Si(001) substrates (Ge-VS)[24] using a reactive gas source epitaxy process adapted to an industrial reduced pressure chemical vapor deposition (RP-CVD) reactor with showerhead technology, process temperatures in the 350°C to 375°C range, and Ge_2H_6 and $SnCl_4$ as precursor gases.[25,26] In contrast to the approach of Chen et al.[23] where pseudomorphic and, thus, highly compressively strained and indirect GeSn/Ge quantum well structures were used, the active layers of the laser cavities presented here are grown with thicknesses far beyond the critical thickness for strain relaxation. This – as we showed previously[19,20] – allows to cross the indirect-to-direct bandgap transition while maintaining a high crystalline quality. GeSn alloys with Sn concentrations of 8.5 at.% (sample A) and 12.5 at.% (sample B) with thicknesses of 800 nm and 560 nm, respectively, are used for microdisk fabrication (Fig. 1a). X-ray diffraction reciprocal space maps (XRD-RSM) reveal residual compressive biaxial strain values of -0.15 % (sample A) and -0.40 % (sample B), respectively.
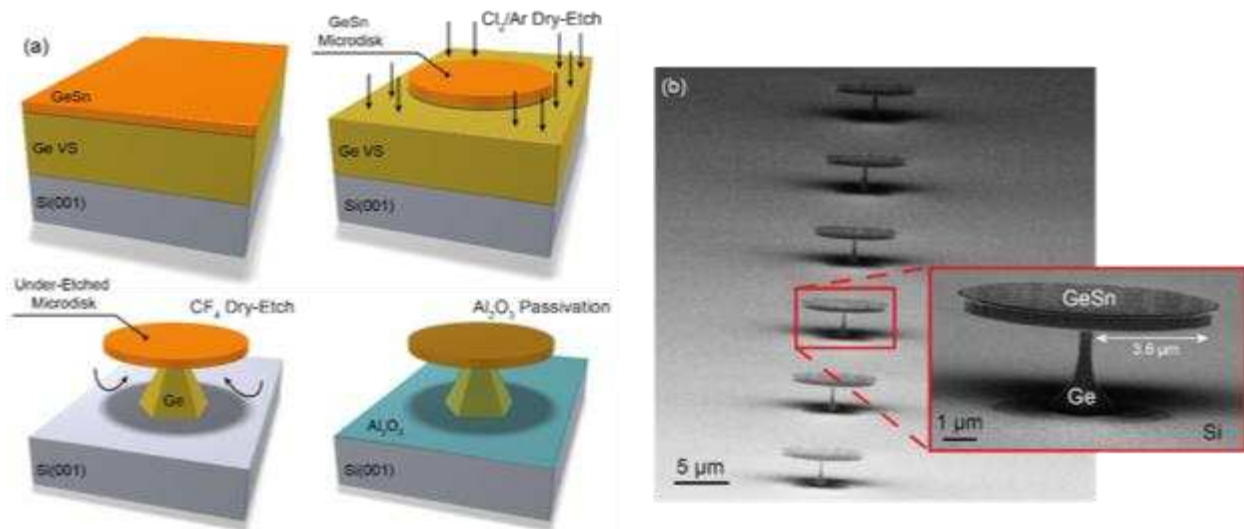
Figure 1. Fabrication of GeSn microdisks (a) Schematic representation of the fabrication flow and (b) scanning electron micrograph (SEM) of 8 µm diameter $Ge_{0.875}Sn_{0.125}$ microdisks with the underlying Ge-VS undercut by 3.6 µm.

The GeSn mesa with diameters ranging from 8 µm to 140 µm are defined by standard Si processing as shown in Fig. 1a: e-beam lithography is followed by reactive ion etching using a Cl_2/Ar plasma. In a subsequent step, the Ge-VS underneath the GeSn layer is selectively removed by isotropic CF_4 dry etch[27] resulting in an free standing rim of the microdisk adjoined to the Ge pedestal. Finally, to reduce surface recombination, 10 nm Al_2O_3 is conformally deposited in order to passivate the surface[28,29] using an optimized CMOS high-k passivation process by means of atomic layer deposition (ALD) at 300°C. A scanning electron micrograph (SEM) showing an array of processed GeSn microdisks is presented in Fig. 1b.

We expect that undercutting the GeSn disks will improve the optical properties of the cavity in two ways: (i) enhancement of the optical confinement by increasing the refractive index contrast between the active GeSn and the surrounding medium (air); (ii) a favorable distribution of the electrons between L- and the optically active Γ-valley from their enlarged energy separation via strain relaxation. To investigate the effect of strain relaxation we compare microdisks with 8 μm and 20 μm diameter. For the smaller ones, the remaining Ge pedestal is narrow (800 nm diameter -Fig. 1b) such that the GeSn disks elastically relax and are thus almost strain free, as is verified by mechanical simulations (cf. SI Fig. S1a). Instead, mechanical constraints due to anchoring of the larger microdisks to larger Ge pedestals (13 μm diameter) lead to residual compressive uniaxial strain in the undercut region along the azimuthal direction, as demonstrated in the following.

Strain measurement. The compressive strain of the epitaxial $Ge_{0.875}Sn_{0.125}$ layer was measured using X-ray diffraction spectroscopy (XRD) to be -0.4 %. The local strain distribution is investigated by μ-Raman spectroscopy on a 20 μm diameter microdisk undercut by 3.5 μm. Here fore, a WiTec system including a 532 nm laser with a spot size of approx. 500 nm is used. As expected, the measured Raman peak shifts towards lower wavenumbers towards the edge of the disk, evidencing a strain gradient with a maximum compressive strain in the middle of the structure due to anchoring to the Ge pedestal (see SI, Fig. S2).

We modeled the strain relaxation of the partially undercut microdisks using COMSOL multi-physics. The results for the 20 μm diameter microdisks with an undercut of 3.5 μm are shown in Fig. 2a-c. While both in-plane strain components ε_{xx} and ε_{yy} depend on the azimuthal angle and

the strain deviates from biaxial strain (i.e., $\varepsilon_{xx} \neq \varepsilon_{yy}$), $\varepsilon_{xx} + \varepsilon_{yy}$ only depends on the radius as expected from the cylindrical geometry of the problem. The strain, as intended, decays towards the periphery of the disk. The resulting morphing of the band structure at room temperature (RT) is calculated using the 8 band k·p method and is shown in Fig. 2d. The direct bandgap decreases by 20 meV while moving from the center of the microdisk to the point with the smallest bandgap close to the rim of the microdisk. The energy difference between the L- and Γ- valleys is found to increase from 52 meV up to 78 meV. This increased directness (the difference between L- and Γ-valley) together with the bandgap narrowing are expected to enhance the PL at the circumference. The increased L- to Γ-valley separation enhances the percentage of the electron population residing in the Γ-valley. The bandgap narrowing results in an effective field gradient enhancing free carrier concentrations towards the periphery of the microdisk where the WGM have the highest intensity. Unfortunately, the strain enlarges the valence band splitting in the center of the disk forming an energy minimum for holes. Still, the net effect of the bandgap narrowing results in a modest enhancement of both electron and hole concentrations towards the periphery of the microdisk, as shown in the SI (Fig. S3). The carrier concentrations are calculated by solving the self-consistent drift-diffusion equations assuming electron and hole mobilities of 100 cm^2/Vs[30] and a carrier generation rate of 2×10^{28} cm^{-3}s^{-1} representing the experimental injection conditions at threshold. The magnitude of the carrier concentration enhancement is quite sensitive to the assumed carrier lifetime and varies between 37% for long lived carriers (> 100 ns), 10 % for a 1 ns carrier lifetime and 2 % for a 100 ps carrier lifetime. Assuming the 2 ns typical carrier lifetime of Ge grown on Si as a likely order of magnitude,[31] a max. 10 % carrier enhancement then appears to be realistic.
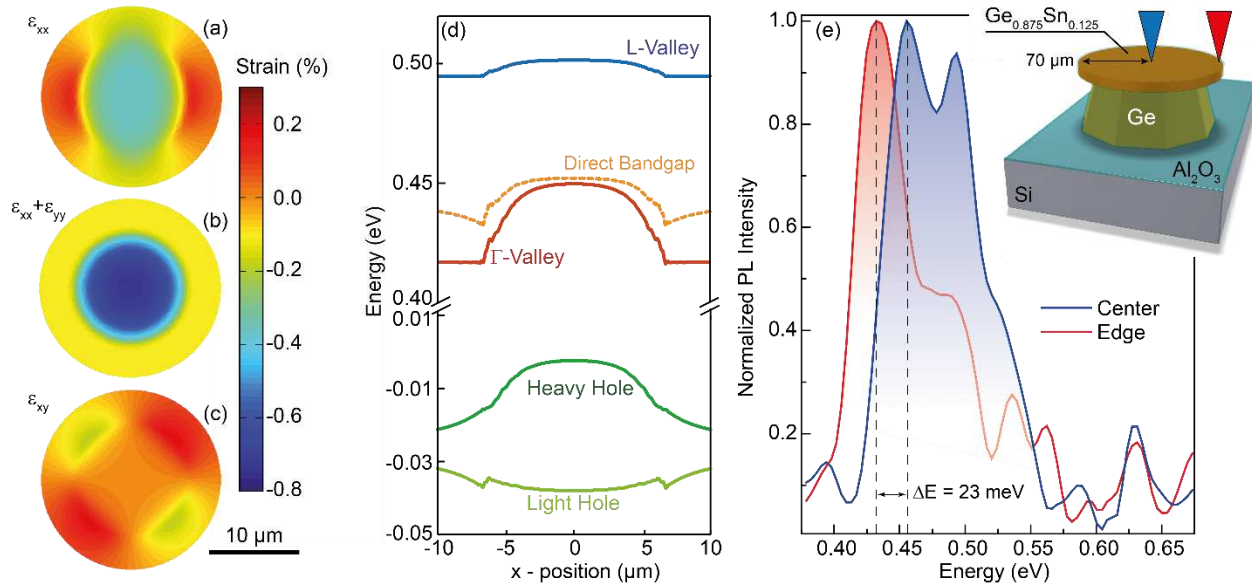
Figure 2. Strain in microdisks with undercut (a), (b) and (c) show color maps of the modeled strain components ε_{xx}, $\varepsilon_{xx}+\varepsilon_{yy}$ and ε_{xy} across the center plane of the microdisk (20 μm diameter, 3.5 μm undercut), respectively. (d) Calculated energies at RT for the two upper strain split valence bands, as well as conduction band Γ-valley and L-valley electrons. The direct bandgap energy is depicted as an orange dotted line. The labels "Heavy Hole" and "Light Hole" apply for the compressively biaxially strained center region of the microdisk, but not for the microdisk periphery where the symmetry of the biaxial strain is broken. (e) RT μ-PL spectra measured at the edge and at the center of a 140 µm Ge$_{0.875}$Sn$_{0.125}$ microdisk (sample B) with 3.7 μm undercut.

A further aspect related to strain relaxation predicted by mechanical simulations is that the biaxial compressive strain at the center of the microdisk (ε_{xx} = -0.37 %, ε_{yy} = -0.37 %, ε_{zz} = +0.26 %) is converted into a compressive uniaxial strain along the azimuthal direction at the

9

periphery of the disk, $\varepsilon_{\theta\theta} = -0.14$ %. The strain component along the radial direction, as well as the one along z are very small, i.e., $\varepsilon_r = \varepsilon_{zz} = +0.038$ %. At cryogenic temperatures, at which the resulting 11 meV splitting between the two topmost valence bands is sufficient to play a role, this strain actually enhances the gain for modes with the E-fields oriented along the compressively strained azimuthal direction[32] but is unfavorable for the amplification of WGMs with their E-field oriented either along the radial direction for transverse electric (TE) modes, or along the z-direction for transverse magnetic (TM) modes.

For the smaller, 8 µm diameter undercut microdisks (see SI Fig. S1b) the strain behavior is very different because the pedestal is much smaller (800 nm diameter) and, therefore, does not constitute a significant mechanical constrain. In fact, the pedestal deforms to accommodate the strain relaxation of the GeSn disk, so that the latter is almost fully relaxed ($\varepsilon_{\theta\theta} = 1.9 \times 10^{-5}$).

The experimental verification of the reduced bandgap due to strain relaxation is carried out by spatially resolved (ca. 10 µm resolution) RT µ-PL. The experiment is performed on a larger (140 µm diameter) $Ge_{0.875}Sn_{0.125}$ microdisk with a nearly identical 3.7 µm undercut using a continuous wave solid-state laser emitting at 532 nm with a power below 1.5 mW focused onto a spot size of approx. 10 µm. An expected red shift is obvious when comparing spectra acquired at the center and at the edge of the disk (Fig. 2e). The two dominant µ-PL peaks recorded at the center of the disk, at 0.46 eV and 0.49 eV, match well the predictions from band diagram calculations (0.4521 eV and 0.4876 eV, corresponding to the transitions between the Γ-valley and the heavy and light holes, respectively, in the central biaxially strained region of the microdisk). The red shift of the peaks at the circumference of the microdisk to 0.44 eV for the dominant, lower energy peak

is in agreement with the calculated bandgap narrowing observed at the edge of the disk in Fig. 2d, even though the magnitude of the experimentally observed shift slightly exceeds that of the calculations, 23 meV versus 19.6 meV, respectively.
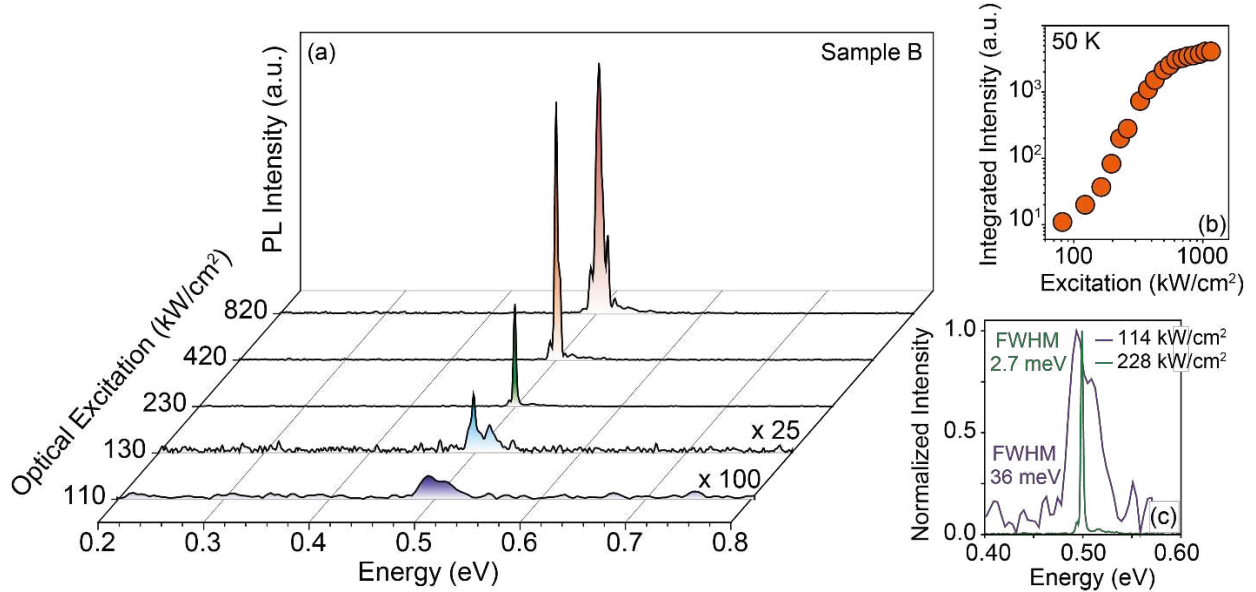

Figure 3. Optical characteristics of microdisk lasers with an 8 µm diameter (a) PL spectra of a microdisk resonator from sample B for different optical excitation densities at 50 K. (b) Light-in light-out curve (LL curve) as well as (c) linewidth narrowing obtained above the lasing threshold.

Characterization of GeSn microdisk lasers. Microdisk resonators with an 8 µm diameter are optically excited using a pulsed (5 ns) Nd:YAG laser with a center wavelength of 1064 nm and a repetition rate of 17 kHz. The Full Width at Half Maximum (FWHM) of the excitation spot has been determined to be 10 µm, ensuring excitation of the whole disk. The PL spectra of a microdisk from sample B are shown in Fig. 3a at 50 K as a function of optical excitation levels. The device emits light with photon energies around 0.5 eV ($\lambda\sim2.5$ µm). For excitation densities above

200 kW/cm^2 the intensity of the luminescence increases abruptly, indicating a lasing threshold. In Fig. 3b the integrated PL intensity as a function of excitation, known as the light-in light-out (LL) curve, features a clear S-shape with a lasing threshold at approx. 220 kW/cm^2. At high pumping levels the laser intensity saturates, which we attribute to heating. Electron-hole pairs are excited in the free standing resonators at high energy 1.17 eV exceeding the ~0.5 eV bandgap by 0.67 eV. The absence of an efficient heat sink in the suspended structure thus will lead to heating. Above the lasing threshold[33] the resonance linewidth collapses as expected (Fig. 3c).
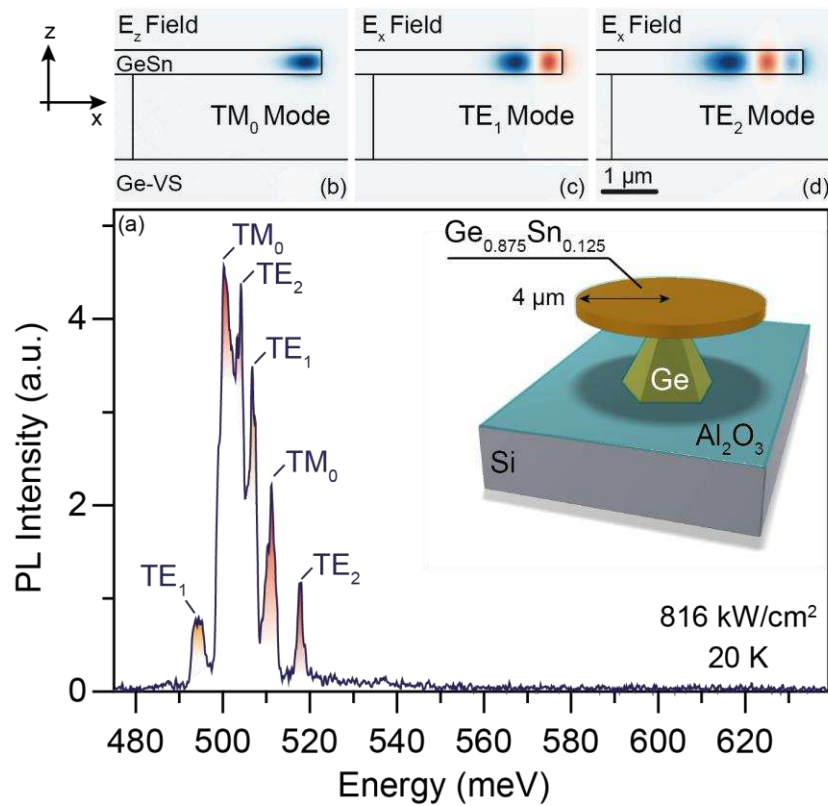
Figure 4. Microdisk modes: (a) High resolution μ-PL spectrum of an 8 µm diameter microdisk of sample B taken at 20 K under an excitation (816 kW/cm^2) well above threshold featuring multi-mode lasing. The peaks are labeled according to their classification in spatial modes. (b) E_z-field of the TM$_0$ mode, (c) E_x-field of the TE$_1$ mode and (d) E_x-field of the TE$_2$ mode.

Whispering gallery modes. Fig. 4a shows a spectrum of an 8 µm diameter microdisk from sample B taken with a spectral resolution of approx. 0.25 meV, excited at 816 kW/cm^2 at 20 K. The multi-mode emission of the laser consists of several peaks with central emission energies at $\omega_a = 0.4944$ eV, $\omega_b = 0.5003$ eV, $\omega_c = 0.5042$ eV, $\omega_d = 0.5067$ eV, $\omega_e = 0.5111$ eV, and $\omega_f = 0.5178$ eV. Optical simulations were performed with Synopsys RSoft in order to determine the group index n_g, free spectral range (FSR) and overlap Γ_m of the lowest TE-polarized and TM-polarized WGMs with the active GeSn layer. Results are summarized in Table S1. The corresponding modes are depicted in Fig. 4b, c and d. It should be noted that due to the small radii of the microdisks, a corrective factor was introduced in the usual formula of the overlap in order to account for the cylindrical geometry, c.f. SI.

It is immediately apparent that the lines in the spectrum of Fig. 4a cannot correspond to the comb of a single spatial WGM mode since they are too closely and irregularly spaced for this to be the case. However, every third line can be attributed to a given family of WGMs corresponding to the same spatial mode, e.g., $\omega_d - \omega_a = 12.3$ meV is consistent with the FSR of TE$_1$ modes at the center wavelength of 2.477 µm, $\omega_e - \omega_b = 10.8$ meV is consistent with the FSR of TM$_0$ modes at

13

the center wavelength of 2.452 µm, and $\omega_f - \omega_c = 13.6$ meV is consistent with the FSR of TE$_2$ modes at the center wavelength of 2.427 µm.

Quality factors extracted from recorded linewidths, of the order of Q = 200 - 400, are much too low to be explained by bending losses and can be related to excess noise, in particular the shot to shot fluctuation of the excitation laser intensities. In fact, the calculated bending losses for the TM$_0$, TE$_1$ and TE$_2$ WGMs are very low, with the highest bending losses for the TE$_2$ mode on the order of 0.3 dB/cm. Thus, round trip losses are dominated by scattering losses and/or absorption losses caused by e.g. material defects, free carrier absorption due to the high free carrier densities associated to the high lasing thresholds, or intervalence band absorption. The assumption of lasing corresponding to WGMs at the strain relaxed periphery of the disk is consistent with PL spectra taken on larger microdisks (sample B, 20 µm diameter, c.f. SI Fig. S4), for which the undercut (4.3 µm) only accounts for a much smaller percentage of the total microdisk area: In these spectra, a spontaneous emission background attributed to emission from the higher compressively strained central region of the disk remains significant even after onset of lasing. The laser emission is red shifted by ~21 meV relative to the spontaneous emission background, in good agreement with the ~23 meV shift observed in the RT µ-PL measurements as well as with the calculated 20 meV strain relaxation induced bandgap narrowing reported above. The small discrepancies can be partially accounted for by the discrete nature of the WGM resonances, by the increased temperature of the microdisk periphery at high pumping levels, as well as by measurement and calculation accuracy limitations.

Temperature dependent lasing. In Fig. 5a the temperature-dependent PL spectra at an excitation density of 820 kW/cm^2 for microdisks fabricated from samples A and B are shown together with the LL-curves taken at different temperatures (Fig. 5b and c). In accordance with the band structure, the wavelength of the lasing emission is blue-shifted to ~ 610 meV (2.0 µm) for sample A because of the lower Sn concentration relative to sample B. The maximum temperature at which lasing is observed decreases from ~130 K for sample B down to ~90 K for sample A, which is ascribed to the smaller energy separation, $\Delta E_{L-\Gamma}$, between the L- and the Γ-valleys, leading to a less favorable distribution of the electrons between these valleys at finite temperatures and the high excitation densities. Indeed, as can be seen in Fig. 5b and c, sample A shows a more pronounced roll-over of the intensity versus laser excitation than sample B, due to a more significant population of the L-valleys. Notably, even though microdisks from sample A require lower temperatures for lasing, they feature significantly lower optical pumping density thresholds (125 kW/cm^2 at 50 K) compared to sample B (220 kW/cm^2 at 50 K) although the film thickness is thicker and the generated carriers consequently spread over a larger volume. A possible explanation might be reduced losses due to surface roughness because of the reduced mode overlap with the surfaces in the thicker film, however, this effect is still under investigation. It might also be related with an increased material quality for layers with lower Sn content as well as the dependence of Auger recombination on bandgap.

Compared to our previous work presented in ref. 19, in which non-undercut Fabry-Perot lasers made out of GeSn layers of identical thickness and composition as sample B were

characterized, here the onset of lasing is at a reduced threshold (130 kW/cm^2 compared to 325 kW/cm^2 in ref. 19, both measured at 20 K). Moreover, the maximum lasing temperature has been improved from ~90 K to ~130 K. We ascribe these improvements to a combination of the increased modal overlap with the GeSn film (1.1 vs. 0.48 for a non-undercut microdisk of identical diameter and GeSn film thickness), to the expected better surface passivation resulting from the Al$_2$O$_3$ ALD layer and, most importantly, to the increased L- to Γ-valley energy separation resulting from strain relaxation. As visual inspection of a TEM cross-section suggests (see SI Fig. S5), improvement of the threshold does not seem to be due to a reduced defect density in the GeSn after undercutting, as the defective GeSn region appears to withstand the under-etching process.
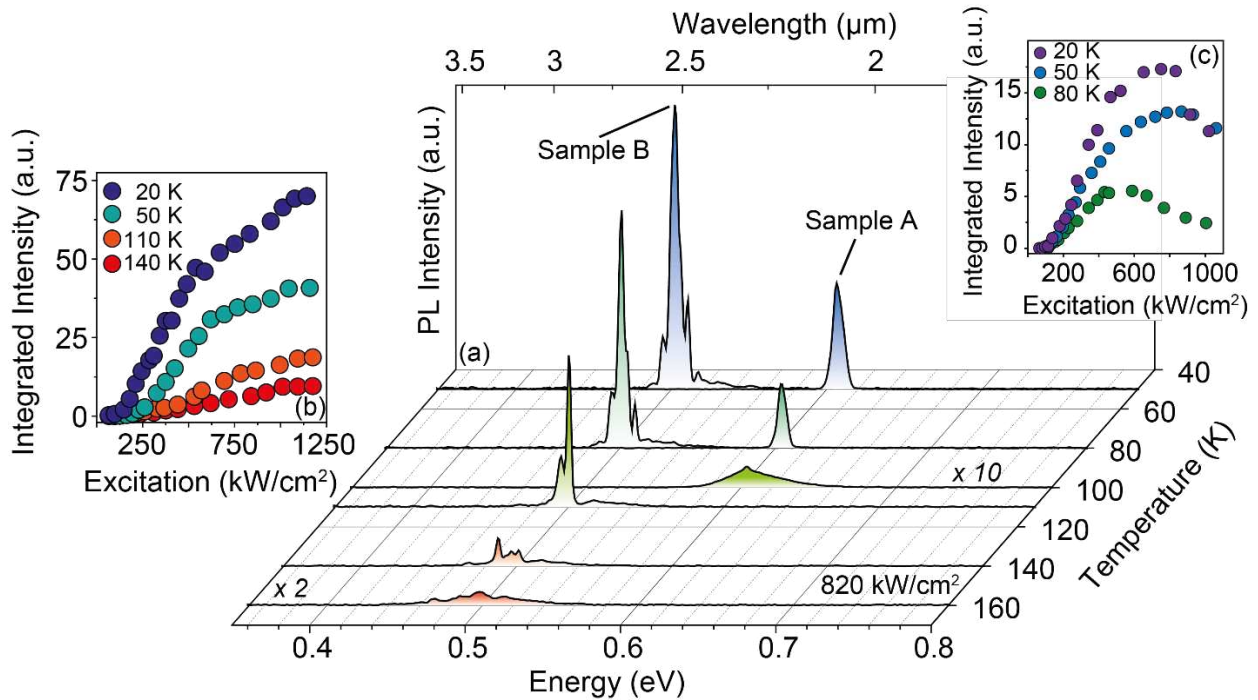
Figure 5. Power and temperature dependence for different Sn contents (a) Temperature-dependent spectra of 8 µm diameter microdisks from sample A and B at 820 kW/cm^2. Light-in light-out curves at different temperatures for (b) sample B and (c) sample A.

The lasing peak from sample B is ~32 meV below the peak observed in ref. 19, presumably due to the strain relaxation occurring here as a result of the undercut. While this is a larger shift than the 23 meV PL shift seen here between the center and the edge of the microdisk due to strain relaxation, the trend is in the right direction. The discrepancy could be due to slight variations in material composition in different samples, carrier density clamping at different levels due to the increased overlap and L- to Γ- valley energy separation, as well as to the increased temperature at the microdisk circumference resulting from reduced heat sinking.

CONCLUSIONS

GeSn microdisk cavities are fabricated and investigated to study the effect of strain and Sn concentration on the lasing properties of group IV GeSn gain material. Owing to a nearly complete strain relaxation in Ge$_{0.875}$Sn$_{0.125}$ and Ge$_{0.915}$Sn$_{0.085}$ microdisks with a diameter of 8 µm - achieved by selective dry etching of the underlying Ge virtual substrate, an improved performance of the laser is obtained. For the devices containing 12.5 at.% Sn the lasing thresholds at 50 K is 220 kW/cm^2 and the maximum lasing temperatures is 130 K. Tuning the Sn concentration results in lasers with emission wavelengths between 2 µm and 2.5 µm, however, the maximum lasing temperature is lowered when decreasing the Sn concentration. This indicates a correlation between

the highest operation temperature and the energy difference between the L- and Γ-valleys. A further increase of the latter by incorporation of higher Sn contents is, thus, expected to result in higher lasing temperatures, constituting a path to improvement besides the routes of defect engineering and applying a proper heat sink.

Important challenges remain on the path to achieve room temperature electrically pumped lasing in an integrated waveguide based planar photonics technology. Reaching the same free carrier injection rate as with the optically pumped threshold power of 220 kW/cm^2 shown here for Ge$_{0.875}$Sn$_{0.125}$ microdisks at 50 K would require a current density of 190 kA/cm^2 which is almost two orders of magnitude higher than state-of-the-art RT III-V lasers. Improvements may arise from an optimized carrier confinement away from the surface and the misfit dislocation networks by using SiGeSn/GeSn double heterostructures (DHS)[34,35] along with an optimized GeSn strain relaxed buffer technology. Confining the dislocation network at a first thin-film interface remote from the DHS ought to be a primary objective on the path towards more efficient and room temperature lasing. The realization of such an all group IV semiconductor laser diode would finally allow Si photonics to reach its full disruptive potential in application fields such as short range optical interconnects and sensing.

AUTHOR INFORMATION
Corresponding Author
*E-mail: d.stange@fz-juelich.de
*E-mail: d.m.buca@fz-juelich.de

Present Addresses

‡ S.W. is now with IBM Research – Zurich, 8803 Rueschlikon, Switzerland.

R.G. is now with Intel Mobile Communications GmbH – Munich, 85579 Neubiberg, Germany.

Author Contributions

The manuscript was written through contributions of all authors. All authors have given approval

to the final version of the manuscript. * D.S., S.W. and R.G. contributed equally to this work.

ASSOCIATED CONTENT

Supporting Information. Additional information on theoretical simulations and optical mode calculations, as well as Raman and microdisks PL analysis are given in SI file.

REFERENCES

(1)   Soref, R. A.; Buca, D.; Yu, S.-Q. Group IV Photonics- Driving Integrated Optoelectronics. Opt. Photonics News **2016**, January, 32–39.

(2)   Van Campenhout, J.; Binetti, P. R. A.; Romeo, P. R.; Regreny, P.; Seassal, C.; Leijtens, X. J. M.; de Vries, T.; Oei, Y. S.; van Veldhoven, R. P. J.; Notzel, R.; Di Cioccio, Lé.; Fedeli, J.-M.; Smit, M. K.; Van Thourhout, D.; Baets, R. Low-Footprint Optical Interconnect on an SOI Chip Through Heterogeneous Integration of InP-Based Microdisk Lasers and Microdetectors. IEEE Photonics Technol. Lett. **2009**, 21, 522–524.

(3)   Duan, G.-H.; Jany, C.; Le Liepvre, A.; Accard, A.; Lamponi, M.; Make, D.; Kaspar, P.; Levaufre, G.; Girard, N.; Lelarge, F.; Fedeli, J.; Descos, A.; Ben Bakir, B.; Messaoudene, S.; Bordel, D.; Menezo, S.; de Valicourt, G.; Keyvaninia, S.; Roelkens, G.; Van

Thourhout, D.; Thomson, D. J.; Gardes, F. Y.; Reed, G. T. Hybrid III--V on Silicon Lasers for Photonic Integrated Circuits on Silicon. IEEE J. Sel. Top. Quantum Electron. **2014**, 20, 158–170.

(4)   Roelkens, G.; Abassi, A.; Cardile, P.; Dave, U.; Groote, A. De; Koninck, Y. De; Fu, X.; Gassenq, A.; Hattasan, N.; Huang, Q.; Kumari, S.; Keyvaninia, S.; Kuyken, B.; Li, L.; Mechet, P.; Muneeb, M.; Sanchez, D.; Shao, H.; Spuesens, T.; Subramanian, A. Z.; Uvin, S.; Tassaert, M.; Gasse, K. Van; Verbist, J.; Wang, R.; Wang, Z.; Zhang, J.; Campenhout, J. Van; Yin, X.; Bauwelinck, J.; Morthier, G.; Baets, R.; Thourhout, D. Van. III-V-on-Silicon Photonic Devices for Optical Communication and Sensing. Photonics **2015**, 2, 969–1004.

(5)   Chen, S.; Li, W.; Wu, J.; Jiang, Q.; Tang, M.; Shutts, S.; Elliott, S. N.; Sobiesierski, A.; Seeds, A. J.; Ross, I.; Smowton, P. M.; Liu, H. Electrically Pumped Continuous-Wave III–V Quantum Dot Lasers on Silicon. Nat. Photonics **2016**, 10, 307–311.

(6)   Masini, G.; Sahni, S.; Capellini, G.; Witzens, J.; Gunn, C. High-Speed Near Infrared Optical Receivers Based on Ge Waveguide Photodetectors Integrated in a CMOS Process. Adv. Opt. Technol. **2008**, 2008, 1–5.

(7)   Thomson, D. J.; Shen, L.; Ackert, J. J.; Huante-Ceron, E.; Knights, A. P.; Nedeljkovic, M.; Peacock, A. C.; Mashanovich, G. Z. Optical Detection and Modulation at 2µm-2.5µm in Silicon. Opt. Express **2014**, 22, 10825–10830.

(8)   Ackert, J. J.; Thomson, D. J.; Shen, L.; Peacock, A. C.; Jessop, P. E.; Reed, G. T.; Mashanovich, G. Z.; Knights, A. P. High-Speed Detection at Two Micrometres with Monolithic Silicon Photodiodes. Nat. Photonics **2015**, 9, 393–396.

(9)   Gill, D. M.; Xiong, C.; Proesel, J.; Rosenberg, J.; Ellis-Monaghan, J.; Orcutt, J.; Khater, M.; Viens, D.; Vlasov, Y. A.; Haensch, W.; Green, W. Demonstration of Error Free Operation Up To 32 Gb/s From a CMOS Integrated Monolithic Nano-Photonic Transmitter. In CLEO: 2015; OSA: Washington, D.C., 2015; p STu4F.3.

(10) Romero-García, S.; Merget, F.; Zhong, F.; Finkelstein, H.; Witzens, J. Silicon Nitride CMOS-Compatible Platform for Integrated Photonics Applications at Visible Wavelengths. Opt. Express **2013**, 21, 14036.

(11) Sieger, M.; Mizaikoff, B. Toward On-Chip Mid-Infrared Sensors. Anal. Chem. **2016**, 88, 5562–5573.

(12) Homewood, K. P.; Lourenço, M. a. Optoelectronics: The Rise of the GeSn Laser. Nat. Photonics **2015**, 9, 78–79.

(13) Liang, D.; Bowers, J. E. Recent Progress in Lasers on Silicon. Nat. Photonics **2010**, 4, 511–517.

(14) Muneeb, M.; Chen, X.; Verheyen, P.; Lepage, G.; Pathak, S.; Ryckeboer, E.; Malik, A.; Kuyken, B.; Nedeljkovic, M.; Van Campenhout, J.; Mashanovich, G. Z.; Roelkens, G. Demonstration of Silicon-on-Insulator Mid-Infrared Spectrometers Operating at 3.8µm.

Opt. Express **2013**, 21, 11659.

(15) Liu, J.; Sun, X.; Camacho-Aguilera, R.; Kimerling, L. C.; Michel, J. Ge-on-Si Laser Operating at Room Temperature. Opt. Lett. **2010**, 35, 679–681.

(16) Süess, M. J.; Geiger, R.; Minamisawa, R. A.; Schiefler, G.; Frigerio, J.; Chrastina, D.; Isella, G.; Spolenak, R.; Faist, J.; Sigg, H. Analysis of Enhanced Light Emission from Highly Strained Germanium Microbridges. Nat. Photonics **2013**, 7, 466–472.

(17) Sanchez-Perez, J. R.; Boztug, C.; Chen, F.; Sudradjat, F. F.; Paskiewicz, D. M.; Jacobson, R.; Lagally, M. G.; Paiella, R. Direct-Bandgap Light-Emitting Germanium in Tensilely Strained Nanomembranes. Proc. Natl. Acad. Sci. **2011**, 108, 18893–18898.

(18) Sukhdeo, D. S.; Nam, D.; Kang, J.-H.; Brongersma, M. L.; Saraswat, K. C. Direct Bandgap Germanium-on-Silicon Inferred from 5.7 % (100) Uniaxial Tensile Strain. Photonics Res. **2014**, 2, A8.

(19) Wirths, S.; Geiger, R.; von den Driesch, N.; Mussler, G.; Stoica, T.; Mantl, S.; Ikonic, Z.; Luysberg, M.; Chiussi, S.; Hartmann, J. M.; Sigg, H.; Faist, J.; Buca, D.; Grützmacher, D. Lasing in Direct-Bandgap GeSn Alloy Grown on Si. Nat. Photonics **2015**, 9, 88–92.

(20) Stange, D.; Wirths, S.; von den Driesch, N.; Mussler, G.; Stoica, T.; Ikonic, Z.; Hartmann, J. M.; Mantl, S.; Grützmacher, D.; Buca, D. Optical Transitions in Direct-Bandgap Ge 1–X Sn X Alloys. ACS Photonics **2015**, 2, 1539–1545.

(21) Ghrib, A.; El Kurdi, M.; Prost, M.; Sauvage, S.; Checoury, X.; Beaudoin, G.; Chaigneau, M.; Ossikovski, R.; Sagnes, I.; Boucaud, P. All-Around SiN Stressor for High and Homogeneous Tensile Strain in Germanium Microdisk Cavities. Adv. Opt. Mater. **2015**, 3, 353–358.

(22) Prost, M.; El Kurdi, M.; Ghrib, A.; Sauvage, S.; Checoury, X.; Zerounian, N.; Aniel, F.; Beaudoin, G.; Sagnes, I.; Boeuf, F.; Boucaud, P. Tensile-Strained Germanium Microdisk Electroluminescence. Opt. Express **2015**, 23, 6722.

(23) Chen, R.; Gupta, S.; Huang, Y.; Huo, Y.; Rudy, C. W.; Sanchez, E.; Kim, Y.; Kamins, T. I.; Saraswat, K. C.; Harris, J. S. Demonstration of a Ge/GeSn/Ge Quantum-Well Microdisk Resonator on Silicon: Enabling High-Quality Ge(Sn) Materials for Micro- and Nanophotonics. Nano Lett. **2014**, 14, 37–43.

(24) Hartmann, J. M.; Abbadie, A.; Cherkashin, N.; Grampeix, H.; Clavelier, L. Epitaxial Growth of Ge Thick Layers on Nominal and 6° off Si(001); Ge Surface Passivation by Si. Semicond. Sci. Technol. **2009**, 24, 055002.

(25) von den Driesch, N.; Stange, D.; Wirths, S.; Mussler, G.; Holländer, B.; Ikonic, Z.; Hartmann, J. M.; Stoica, T.; Mantl, S.; Grützmacher, D.; Buca, D. Direct Bandgap Group IV Epitaxy on Si for Laser Applications. Chem. Mater. **2015**, 27, 4693–4702.

(26) Wirths, S.; Tiedemann, a. T.; Ikonic, Z.; Harrison, P.; Holländer, B.; Stoica, T.; Mussler, G.; Myronov, M.; Hartmann, J. M.; Grützmacher, D.; Buca, D.; Mantl, S. Band Engineering and Growth of Tensile Strained Ge/(Si)GeSn Heterostructures for Tunnel

Field Effect Transistors. Appl. Phys. Lett. **2013**, 102, 192103.

(27) Gupta, S.; Chen, R.; Huang, Y.-C.; Kim, Y.; Sanchez, E.; Harris, J. S.; Saraswat, K. C. Highly Selective Dry Etching of Germanium over Germanium-Tin (Ge1-xSnx): A Novel Route for Ge1-xSnx Nanostructure Fabrication. Nano Lett. **2013**, 13, 3783–3790.

(28) Wirths, S.; Stange, D.; Pampillón, M.-A.; Tiedemann, A. T.; Mussler, G.; Fox, A.; Breuer, U.; Baert, B.; San Andrés, E.; Nguyen, N. D.; Hartmann, J.-M.; Ikonic, Z.; Mantl, S.; Buca, D. High- K Gate Stacks on Low Bandgap Tensile Strained Ge and GeSn Alloys for Field-Effect Transistors. ACS Appl. Mater. Interfaces **2015**, 7, 62–67.

(29) Gupta, S.; Chen, R.; Harris, J. S.; Saraswat, K. C. Atomic Layer Deposition of Al2O3 on Germanium-Tin (GeSn) and Impact of Wet Chemical Surface Pre-Treatment. Appl. Phys. Lett. **2013**, 103, 241601.

(30) Nakatsuka, O.; Tsutsui, N.; Shimura, Y.; Takeuchi, S.; Sakai, A.; Zaima, S. Mobility Behavior of Ge 1- X Sn X Layers Grown on Silicon-on-Insulator Substrates. Jpn. J. Appl. Phys. **2010**, 49, 04DA10.

(31) Geiger, R.; Frigerio, J.; Süess, M. J.; Chrastina, D.; Isella, G.; Spolenak, R.; Faist, J.; Sigg, H. Excess Carrier Lifetimes in Ge Layers on Si. Appl. Phys. Lett. **2014**, 104, 062106.

(32) Adams, A. R. Strained-Layer Quantum-Well Lasers. IEEE J. Sel. Top. Quantum Electron. **2011**, 17, 1364–1373.

(33) Samuel, I. D. W.; Namdas, E. B.; Turnbull, G. a. How to Recognize Lasing. Nat. Photonics **2009**, 3, 546–549.

(34) Sun, G.; Soref, R. a; Cheng, H. H. Design of a Si-Based Lattice-Matched Room-Temperature GeSn/GeSiSn Multi-Quantum-Well Mid-Infrared Laser Diode. Opt. Express **2010**, 18, 19957–19965.

(35) Stange, D.; von den Driesch, N.; Rainko, D.; Schulte-Braucks, C.; Wirths, S.; Mussler, G.; Tiedemann, A. T.; Stoica, T.; Hartmann, J. M.; Ikonic, Z.; Mantl, S.; Grützmacher, D.; Buca, D. Study of GeSn Based Heterostructures: Towards Optimized Group IV MQW LEDs. Opt. Express **2016**, 24, 1358.